

# On-Tip Polymerization Method for Multimodal Characterization of Nanoparticles with Electron/Ion Imaging and Atom Probe Tomography

Aristide Djoulde, Anup Sharma, Alfred Bekoe Appiagyei, Levi Tegg, Yang Liu, Lian Zhang, Julie M. Cairney, Yunlong Tang, and Jing Fu\*

This work presents a novel method for exploring the structures and chemistry of nanoparticles (NPs), addressing challenges in multimodal and correlative microscopy analysis. The proposed method utilizes a “needle-eye” design, featuring a through-microchannel fabricated at the needle tip. The microchannel and its surface are tuned via focused ion beam (FIB) milling and plasma treatment, enabling NPs dispersed in a resin precursor to be confined in the microchannel due to a pressure gradient upon immersion. The retained suspension is promptly polymerized in situ on the tip and shaped by FIB milling into specific geometries, including but not limited to a micropillar, lamella, and nanoneedle. Here, to demonstrate its applicability, a mixed metal oxide catalyst prepared by the needle-eye approach is characterized with energy-dispersive X-ray spectroscopy (EDX), FIB secondary ion mass spectrometry (FIB-SIMS), (scanning) transmission electron microscopy ((S)TEM), and atom probe tomography (APT). The results validate the ability of the method to achieve multimodal, combining correlative and complementary high-resolution structural and chemical imaging of individuals and clustered NPs. The proposed method confines picoliter-scale samples (6–60 pL) at a tip, eliminating lift-out and microtomy while enabling comprehensive analysis via combined microscopy techniques.

and expanding applications in solar energy conversion, catalysis, drug delivery, imaging, environmental remediation, and medical uses.<sup>[1]</sup> Typically synthesized as powders or in a liquid medium, they exhibit local compositional and structural variations from single nanometers down to smaller molecules and are classified based on their shape into zero-dimensional (0D), one-dimensional (1D), two-dimensional (2D), or three-dimensional (3D) structures.<sup>[2]</sup> Determining their structure and chemical composition in two or three dimensions (2/3D), ideally at the single-particle level and in their native state, is essential for assessing stability, understanding structure-function relationships, and ensuring effective applications.<sup>[3]</sup>

Numerous characterization tools with different spatial resolutions are available to assess detailed high-resolution information for NPs. Methods such as focused ion beam-scanning electron microscopy (FIB-SEM) and (scanning) transmission electron microscopy ((S)TEM), paired

with spectroscopic techniques such as energy-dispersive X-ray spectroscopy (EDX) and electron energy loss spectroscopy (EELS) provide high-resolution ( $\approx 1$  nm for FIB/SEM and less than 0.1 nm for (S)TEM) structural information and elemental analysis.<sup>[4]</sup>

## 1. Introduction

Nanomaterials, particularly nanoparticles (NPs), are a major research focus due to their unique physical and chemical properties

A. Djoulde, A. Sharma, Y. Tang, J. Fu  
Department of Mechanical and Aerospace Engineering  
Monash University  
Clayton, Victoria 3800, Australia  
E-mail: [jing.fu@monash.edu](mailto:jing.fu@monash.edu)

A. Sharma  
Department of Mechanical Engineering  
Indian Institute of Technology Bombay  
Powai, Mumbai 400076, India  
A. B. Appiagyei, L. Zhang  
Department of Chemical and Biological Engineering  
Monash University  
Clayton, Victoria 3800, Australia  
L. Tegg, J. M. Cairney  
School of Aerospace  
Mechanical and Mechatronic Engineering  
University of Sydney  
Camperdown, NSW 2006, Australia  
Y. Liu  
Monash Centre for Electron Microscopy  
Monash University  
Melbourne, Victoria 3800, Australia

The ORCID identification number(s) for the author(s) of this article can be found under <https://doi.org/10.1002/smt.202500622>

© 2025 The Author(s). Small Methods published by Wiley-VCH GmbH. This is an open access article under the terms of the [Creative Commons Attribution-NonCommercial-NoDerivs](#) License, which permits use and distribution in any medium, provided the original work is properly cited, the use is non-commercial and no modifications or adaptations are made.

DOI: 10.1002/smt.202500622

Secondary ion mass spectrometry (SIMS) imaging methods also facilitate characterization at resolutions between tens to hundreds of nanometers, making them effective for analyzing individual nanomaterials.<sup>[5]</sup> The generated 2D information can be further extended to 3D by acquiring a series of micrographs to construct an object in 3D, namely tomography.<sup>[6]</sup> In addition, atom probe tomography (APT) can offer 3D imaging of nanomaterials with exceptional compositional sensitivity at the atomic scale.<sup>[7]</sup> It has recently become a popular technology for reliable quantitative chemical information analysis of single nanosized objects, and it allows for comprehensive 3D morphological and compositional analysis at the near-atomic level when correlated with (S)TEM.<sup>[8]</sup>

All the above-listed techniques require meticulous sample preparation.<sup>[9]</sup> To date, several methods have been proposed: 1) NPs are absorbed onto a TEM grid support film, stained with heavy metal, and dried for TEM imaging;<sup>[10]</sup> 2) NPs are coated on an appropriate substrate via dip coating, spin coating or drop-casting; or embedded in a matrix such as resin, metal. Subsequent FIB milling is routinely used for site-specific thinning from the large substrate, lift-out, and transfer to a half-grid or post using a manipulator for analysis.<sup>[11]</sup> Final FIB milling is used to prepare geometries like thin film (lamella) for (S)TEM, or a sharp needle specimen for correlative APT and (S)TEM analysis.<sup>[12]</sup> 3) Ultramicrotomy offers an alternative by producing thin sections (<100 nm) without requiring any FIB milling.<sup>[13]</sup> 4) For soft or electron-beam-sensitive materials, cryogenic preparation is adopted to solidify the specimen, requiring specialized equipment and multiple detail-centered steps such as rapid freezing, cryo-ultramicrotomy, and cryo-FIB milling before analysis.<sup>[14]</sup> 5) Direct liquid-phase imaging is another option, involving NPs dispersion sandwiched between two thin electron-transparent SiN window membranes or encapsulated in specialized containers that maintain vacuum compatibility needed for electron microscopes.<sup>[15]</sup> While effective and commonly used, these methods are often time-intensive, require expertise, and limit multimodal accessibility and correlative analysis. There is a pressing need to streamline existing processes or develop a novel, adaptable alternative that can accommodate various nanomaterials, facilitating multimodal and correlative analyses across different high-resolution techniques.

Recently, a handful of methods have been proposed to address the above-mentioned challenges. These methods include the production of microtip coupons, half-grids with laser processing,<sup>[16]</sup> in situ SEM micro-nanomanipulation for direct pick-up and placement,<sup>[17]</sup> and preparation by (di)electrophoresis, which employs conductive sharp needles to attract charged particles in a medium.<sup>[18]</sup> Other methods focus on trapping nanomaterials in liquid suspensions, such as graphene encapsulation,<sup>[19]</sup> and rapid vitrification of substrates (copper or gold TEM grid) with pipetted liquid specimens.<sup>[14]</sup> While these methods are innovative, they often suffer from limited reproducibility and low repeatability, highlighting the need for more reliable and standardized methods.

Liquid trapping with needle substrates shows great promise as a simple and effective method for preparing NPs. Early studies explored methods such as dipping open-capillary grooves or nanopores on substrates, leveraging capillary force to naturally drive the fluid into the capillary geometry without any external

power.<sup>[20]</sup> However, challenges such as inefficient volume control, poor liquid retention, rapid evaporation, and large droplet formation around the needle tip complicate volume control and limit their applicability. Closed microchannels provide a good candidate for more reliable flow dynamics and volume control.<sup>[21]</sup> Additionally, these methods have primarily been restricted to water-based analyses through vitrification and suffer from crystalline ice formation during preparation.<sup>[22]</sup> To address these limitations, we sought to develop a robust, repeatable, and versatile method.

In this study, we explore a method, namely Needle-Eye Microtrap (NEM), which employs a needle substrate featuring an eye design (through-microchannel of rectangular cross-section) at the tip to retain a liquid specimen and promptly solidify it for analysis. Specifically, we showcase the capability of the method to retain NPs dispersed in resin precursor and polymerize in the eye design for room-temperature high-resolution studies. A detailed overview of the proposed sample preparation method is schematically illustrated in **Figure 1**. The process involves four key steps: (step 1) fabricating a needle-eye design (closed-microchannel) on a needle tip, and modifying the needle surface using plasma cleaning to remove the oxide layer and improve the hydrophilicity of the needle walls; (step 2) immersing the prepared needle in the resin precursor with suspended NPs and using a low vacuum pump to facilitate air bubbles removal and complete microchannel filling. Optional pre-analysis of the confined liquid can then be performed using optical microscopy; (step 3) On-tip polymerization of the resin-embedded NPs on the needle tip: The confined specimen is polymerized on the tip in situ for room temperature using an oven at 70 °C; and; (step 4) FIB milling to produce final geometries directly on the needle tip such as micropillar, lamella and nanoneedle suitable for advanced 2D/3D characterization techniques. We demonstrate that the presented method effectively preserves NPs while providing detailed insights into their composition and structure. In particular, we showcase its application to a broad range of characterization of the heterogeneous catalyst using high-resolution multimodal investigations, spanning SEM, EDX, FIB-SIMS, (S)TEM, and APT.

## 2. Results

### 2.1. On-Tip Polymerization of Resin-Embedded Catalyst Nanoparticles

A Fe-rich spinel nano-sized catalyst was chosen to demonstrate the proposed method. The catalyst consists of six metal oxides, with an elemental composition of 61.2% Fe, 25.8% Mg, 9.3% Al, 2.8% Ca, 0.5% Mn and 0.3% Ti. The average particle size is  $\approx 51.5 \pm 2.4$  nm, as detailed elsewhere.<sup>[23]</sup> These NPs were prepared following the step-by-step procedure detailed in **Figure 1**, to enable their high-resolution characterization.

**Figure 2a** shows the as-purchased needle tip, and the corresponding needle-eye design (**Figure 2b**), which features a through-microchannel of  $\approx 60\,000\ \mu\text{m}^3$  in volume, created via Ga<sup>+</sup> FIB milling. The milling pattern was centered within the needle tip (**Figure 2a**), leaving a  $\approx 10\ \mu\text{m}$  spacing to the needle edge to prevent premature damage or deformation during the liquid collection process. Following the microchannel fabrication, the needle underwent oxygen plasma surface modification and

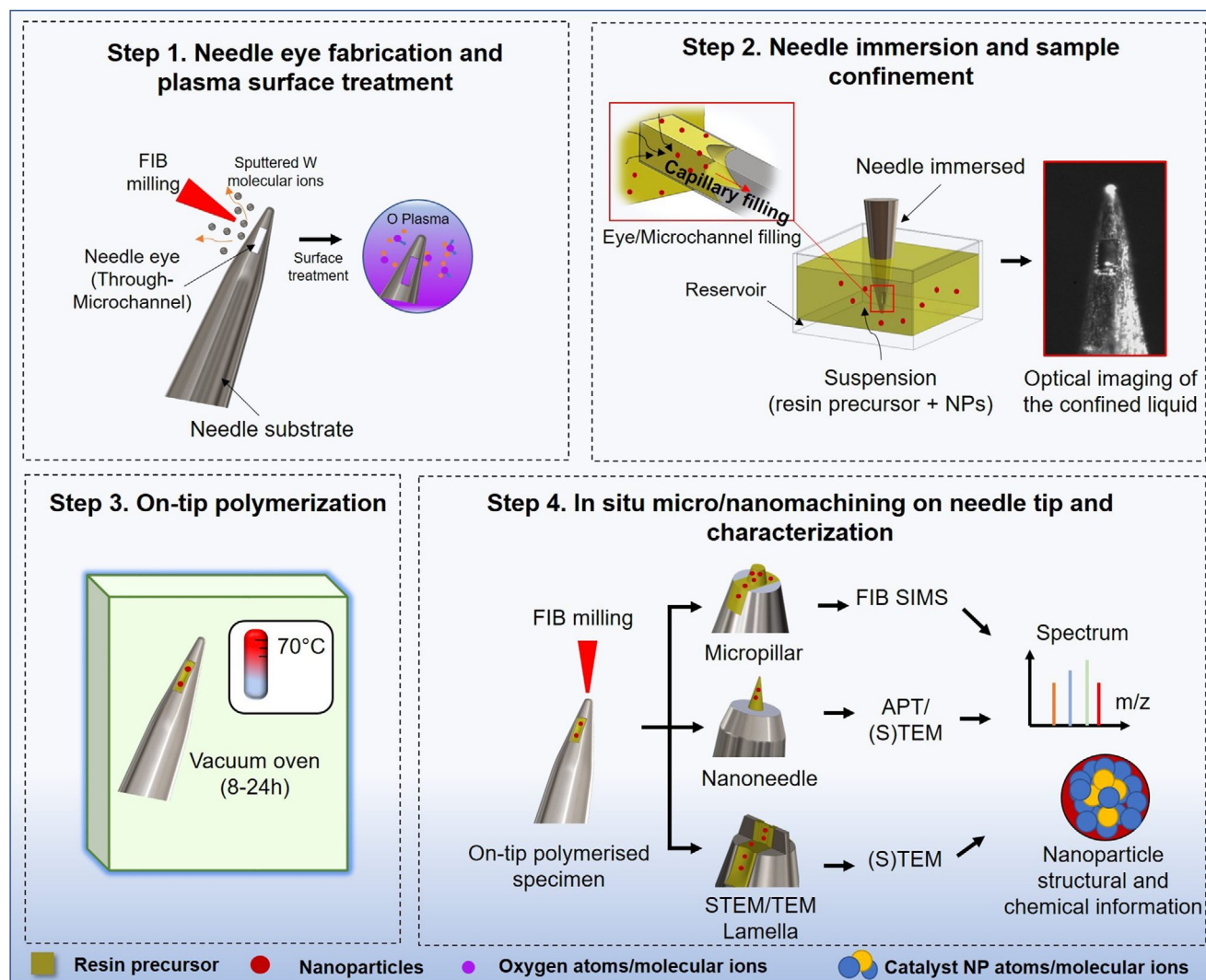
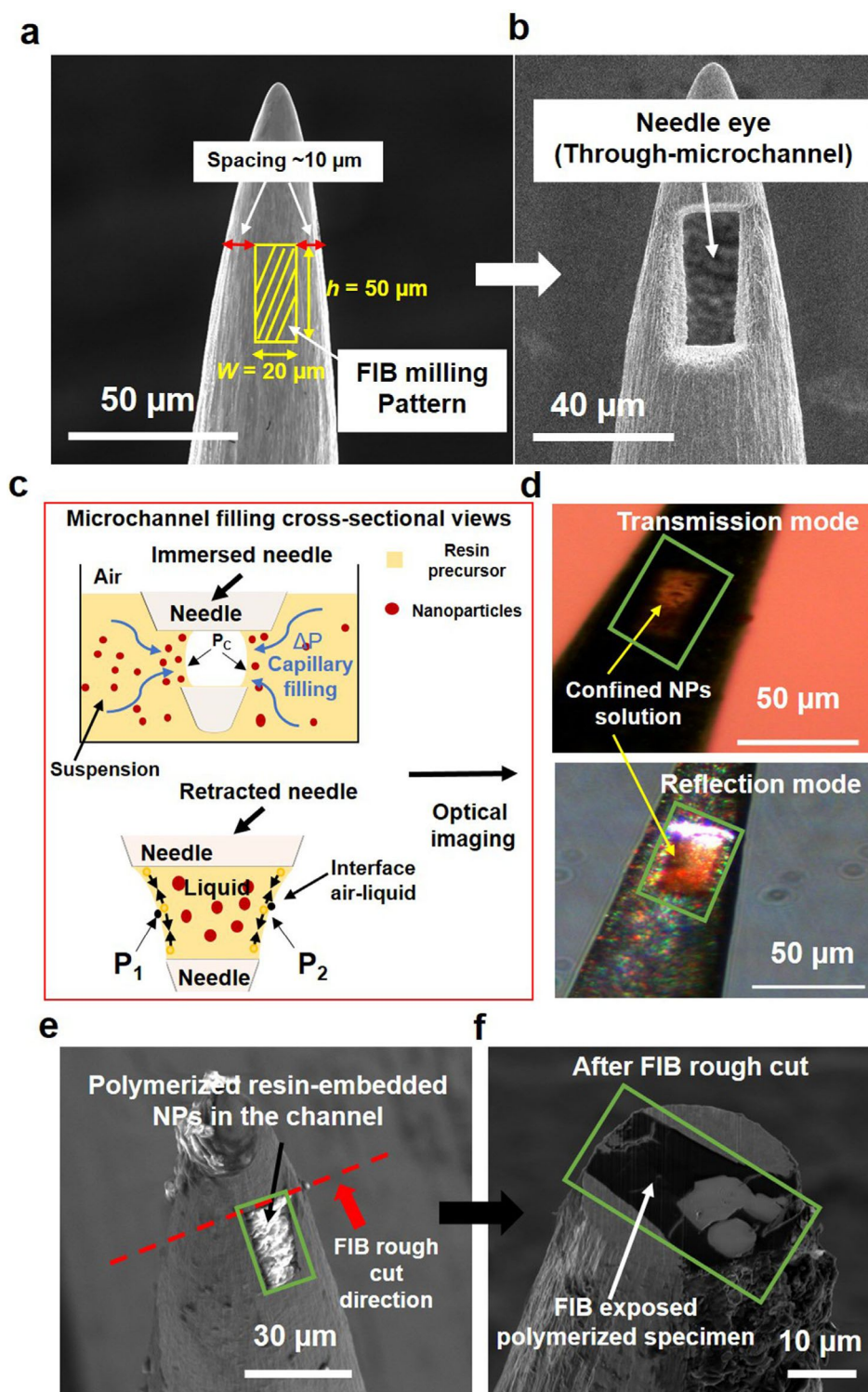


**Figure 1.** Detailed overview of the proposed Needle-Eye Microtrap (NEM) technique which enables on-tip polymerization for multimodal characterization of NPs.

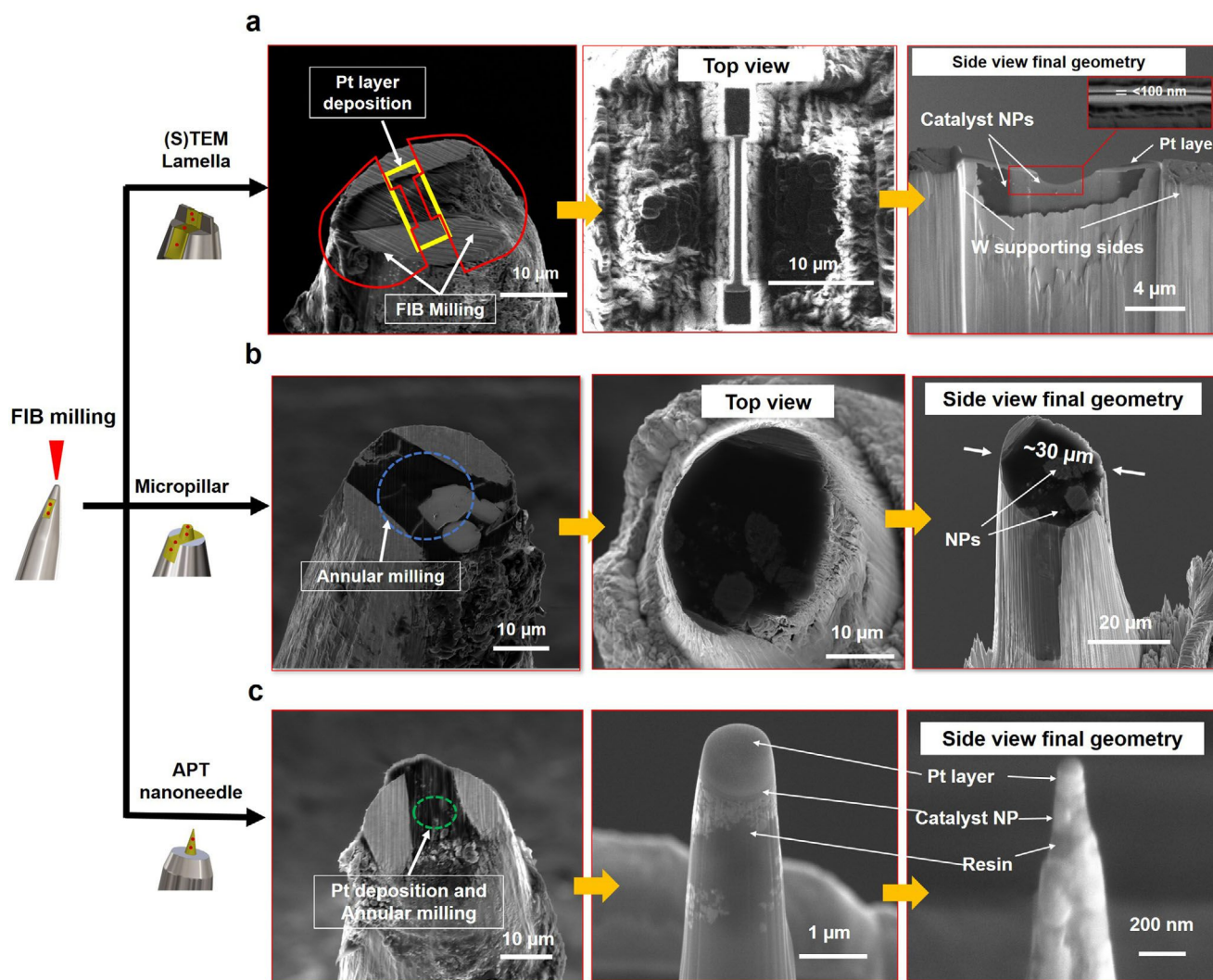
was immersed in a resin precursor containing suspended Fe-rich spinel catalyst to enable through-microchannel filling. Subsequently, a low vacuum chamber at room temperature was used to assist in removing air bubbles, after which the needle was retracted for optical imaging.

Figure 2d shows the optical transmitted and reflected light micrographs, which clearly show the confined liquid in the needle-eye (green boxes) and identifiable particle agglomerations (notably seen in the transmitted light image). We speculate that the filling process is governed by the interplay of a number of factors such as the energy barrier, capillary pressures, gravity, and external forces.<sup>[20,24]</sup> As illustrated in the vertical cross-sectional views in Figure 2c, when the needle is immersed in the liquid suspension, the microchannel is completely soaked, with both ends in contact with the liquid. The capillary pressures,  $P_c$ , at the air-liquid interface within the channel drive the liquid inside, allowing the liquid to spontaneously fill the channel, and a picoliter-sized volume of the suspension is confined. In the

next stage, upon transfer to the vacuum chamber, the external pressure falls below the air bubble's internal pressure, creating a driving pressure gradient  $\Delta P$ . Under this  $\Delta P$ , the air bubbles either diffuse or are expelled. And as the needle is retracted, pressures at  $P_1$  and  $P_2$  at the air-liquid interfaces due to surface tension generate compressive forces that keep the liquid specimen within the microchannel. In addition, strong adhesion of the liquid to the needle's walls helps overcome any imbalance that might otherwise lead to loss of the liquid. This is evidenced by the optical light micrographs in Figure 2d. As the specimen is confirmed within the channel, the needle can be directly placed in the vacuum oven for polymerization. However, to prevent initial evaporation of the retained specimen before polymerization, the needles were immersed in the resin-based suspension and placed in an oven at 70 °C. After 5–7 min of partial polymerization, the needles were carefully removed from the partially hardened resin, followed by a complete polymerization step (8–24 h) to enable high-vacuum room-temperature electron microscopy



**Figure 2.** The proposed NEM enabled catalysts NPs suspended in resin precursor to be confined in the needle-eye design and subsequently polymerized. a-b) Representative SEM images of the W needle tip before (a) and after “eye” (b) fabrication. A rectangular FIB milling pattern of  $w$  ( $20\ \mu\text{m}$ )  $\times$   $h$  ( $50\ \mu\text{m}$ ) is placed at the W needle tip with a spacing of  $\approx 10\ \mu\text{m}$  with the needle edge to remove material, resulting in an eye (through-microchannel). c) Cross-sectional views of the microchannel filling process during immersion, where capillary pressures  $P_c$  due to surface tensions drive the liquid into the channel; and once retracted, a liquid is retained, a consequence of the balance between pressures  $P_1$  and  $P_2$  at the air–liquid interfaces compressing the fluid within the channel. d) Optical investigation: Transmitted and reflected light microscope images of the retracted needle. Specimen confinement is well evidenced (green boxes), confirming the retention of the resin precursor in the microchannel. e) SEM image of the as-polymerized resin-embedded NPs within the microchannel, and f) SEM image after a FIB rough cut to expose the resin.



**Figure 3.** Fabrication of geometries on the needle tip suitable for high-resolution analysis of NPs. a) Representative SEM micrographs showing steps in the fabrication of the lamella, resulting in a thin film with a thickness of less than 100 nm. The yellow rectangle on the initially exposed resin surface indicates a typical region selected for Pt layer deposition, while the red semi-circles mark the areas targeted for FIB milling. b) SEM micrograph of micropillar fabrication. The blue dotted circle denotes the region chosen for annular milling, resulting in a 30 μm micropillar. c) SEM micrograph of APT tip fabrication with a diameter of less than 100 nm. The green dotted circle denotes the region chosen for Pt layer protection and annular milling.

imaging. Figure 2e,f SEM micrographs show the needle after resin polymerization and a FIB cross-section revealing the interior structure of the same needle sample. The images confirm the channel is filled with resin-embedded NPs at the tip. A total of 4 samples ( $n = 4$ ) were prepared following the proposed experimental procedure with micrographs in Figure S1, Supporting Information.

## 2.2. FIB Milling of Designed Geometries on Needle-Tip

The following step in the proposed sample preparation workflow (Figure 1 (step 4)) involves site specific machining on the polymerized specimen on tip. Upon inspection of the resin surface, distinct high-contrast regions were observed, strongly indicating the presence of NPs. The NPs tested in this study primarily

formed clusters, which are expected given their magnetic nature, leading to aggregation within the resin matrix. Consequently, site specific FIB milling is feasible in NP-rich regions.

FIB milling strategies, as presented in the experimental section, were implemented. In this work, geometries including (S)TEM lamella, micropillar, and APT tips were selected for their compatibility with different high-resolution characterization techniques. Figure 3a shows the prepared lamella of ≈100 nm, measured in the middle region of the suspended membrane. To protect the region of interest (ROI) during FIB milling, a thin platinum (Pt) layer was deposited over an initial area of 4 μm × 150 μm using both electron beam (400 nm thick) and ion beam (250 nm thick) deposition. Subsequently, serial FIB millings were performed to cut two trenches, one on each side of the protected region, leaving behind a thin, electron-transparent lamella. The lamella remained supported by the W bulk material on two

opposite sides. The step-by-step micrographs illustrating this fabrication process are provided in Figure S2, Supporting Information.

Figure 3b shows the fabricated micropillar, produced in an area with visible NPs identified by SEM using FIB annular milling. The micropillar had an aspect ratio of 0.9:1 and a target diameter of 30  $\mu\text{m}$ , selected to balance milling time and ion current.

Figure 3c shows an APT tip of  $\approx 100$  nm in diameter was also produced with the sequential milling steps shown in Figure S3, Supporting Information. All the fabricated APT tips after final fine milling were acceptable at this stage and had the NPs positioned in the final shapes and were confirmed in STEM images (Figure S4, Supporting Information).

## 2.3. Structural and Chemical Characterization of Nanoparticles

### 2.3.1. Correlative EDX and FIB-SIMS for Detection and Identification of Resin-Embedded NPs

EDX and FIB-SIMS measurements were performed to obtain detailed information on the chemistry of resin-embedded NPs polymerized on needle tips. The needle featuring a fabricated micropillar (Figure 3b) was selected for these measurements.

Figure 4a shows the SEM micrograph of the FIB-exposed top surface of the micropillar, highlighting the ROI analyzed by EDX, marked by a white box. The corresponding EDX spectra and the quantitative analysis of atomic and weight percentage compositions are provided in Supporting Information (Figure S5 and Table S2, Supporting Information), including EDX data of the as-received NPs. The spectra are predominantly characterized by a strong C signal, alongside other characteristic elements, including O, Mg, Al, Fe, and trace amounts of Ca, with the elemental mapping displayed in Figure 4b. These elements were primarily detected in regions containing NPs, while the C signal was mainly concentrated in the resin matrix. The EDX analysis confirmed the presence of the target elements within the resin-embedded NPs, while some trace amounts of Cl, and Ti were also detected, which are introduced during the NPs synthesis process.<sup>[23]</sup>

The SIMS mass spectrum, corresponding to the analyzed region marked by the red box in Figure 4a, is presented in Figure 4c. An important step in SIMS measurements of multicomponent samples is correctly identifying distinct mass signals for the components of interest due to overlapping signals and determining the optimal primary ion dose for higher spatial resolution. To achieve this, we first analyzed the peaks from the pure resin sample (blue spectrum in Figure 4c) to distinguish pure resin signals from those of the resin-embedded NPs. Ion fragment peaks corresponding to the resin, primarily composed of carbon (C), oxygen (O), oxygen-containing species, and hydrocarbon fragments, were identified at the surface and matched with previously reported spectra.<sup>[12,25]</sup>

The spectrum in red in Figure 4c represents the SIMS spectrum for the resin-embedded NPs sample. The FIB-SIMS imaged region had a measured depth of  $\approx 157.6$  nm, corresponding to a total of  $\approx 500$  frames (with the corresponding SEM image after SIMS acquisition shown in Figure S6, Supporting Information). FIB-SIMS enabled the detection of elemental fragments originat-

ing from the NPs, with tentatively assigned peaks listed in Table S3, Supporting Information (for both resin-embedded NPs and pure resin).

Figure 4d displays SIMS maps of abundant positive ions, whose signals originate from NP-rich regions, attributed to (24)  $\text{Mg}^+$ , (27)  $\text{Al}^+$ , (40)  $\text{Ca}^+$  and (56)  $\text{Fe}^+$ . The FIB-SIMS mapped ion distributions reveal distinct NP patterns, with signals that correlate well with the elemental mapping obtained via EDX. The corresponding depth profile of the analyzed volume is presented in Figure 4e, suggesting a consistent elemental composition, indicating that all NP-forming elements are detectable throughout the depth of the analyzed volume.

### 2.3.2. 3D FIB-SIMS

The elevated geometry of the micropillar at the needle tip made it an ideal candidate for 3D analysis. A 3D FIB-SIMS experiment was also conducted, involving a series of sequential acquisitions. The process involved: an initial acquisition, followed by FIB milling to remove  $\approx 1$   $\mu\text{m}$  of material, exposing a fresh surface for the next SIMS acquisition. This cycle was iterated, with different SIMS acquisition currents, and varying numbers of frames were tested, enabling progressive 3D chemical reconstruction. Detailed experimental parameters are provided in the experimental section.

In total, seven acquisitions were performed, including the first acquisition shown in Figure 4. The SEM images of the needles (in the  $x$ - $z$  plane) recorded before and after the seven SIMS acquisitions (Figure 5a) illustrate a milled depth of  $\approx 7$   $\mu\text{m}$ , while the overall mass spectra are presented in Figure 5b.

Figure 5c presents a 3D reconstructed volume, illustrating the evolution of the spatial distribution of (27)  $\text{Al}^+$ , (24)  $\text{Mg}^+$ , (56)  $\text{Fe}^+$ , and (40)  $\text{Ca}^+$  ions within the micropillar, with the  $z$ -direction representing the discrete SIMS acquisitions. The 3D FIB-SIMS analysis suggests that the constituent elements of the NPs were consistently detected at the surface of the resin-embedded NPs during each SIMS acquisition, indicating that the NPs were distributed at varying depths within the resin matrix. This observation supports the hypothesis that clusters of NPs are dispersed throughout the resin matrix, although not uniformly. Additionally, SEM images of the top surface of the micropillar ( $x$ - $y$  plane) captured before each SIMS acquisition enabled the 3D reconstruction shown in Figure 5d, demonstrating the FIB-slice and view capability on the needle sample.

### 2.3.3. Imaging of Individual Catalyst NPs Prepared in Resin Lamella with STEM

STEM-in-SEM experiment was conducted for structural analysis (size, shape, and distribution) of individual/cluster NPs in the fabricated resin lamella on the needle tip (Figure 3a). As illustrated in Figure 6a, the prepared needle sample featuring the lamella on its tip was attached to the STEM-in-SEM holder and subsequently positioned on the SEM stage. This imaging technique is similar to TEM, leveraging the FIB/SEM system's retractable STEM detector to perform low-voltage STEM, combining the benefits of both SEM and TEM

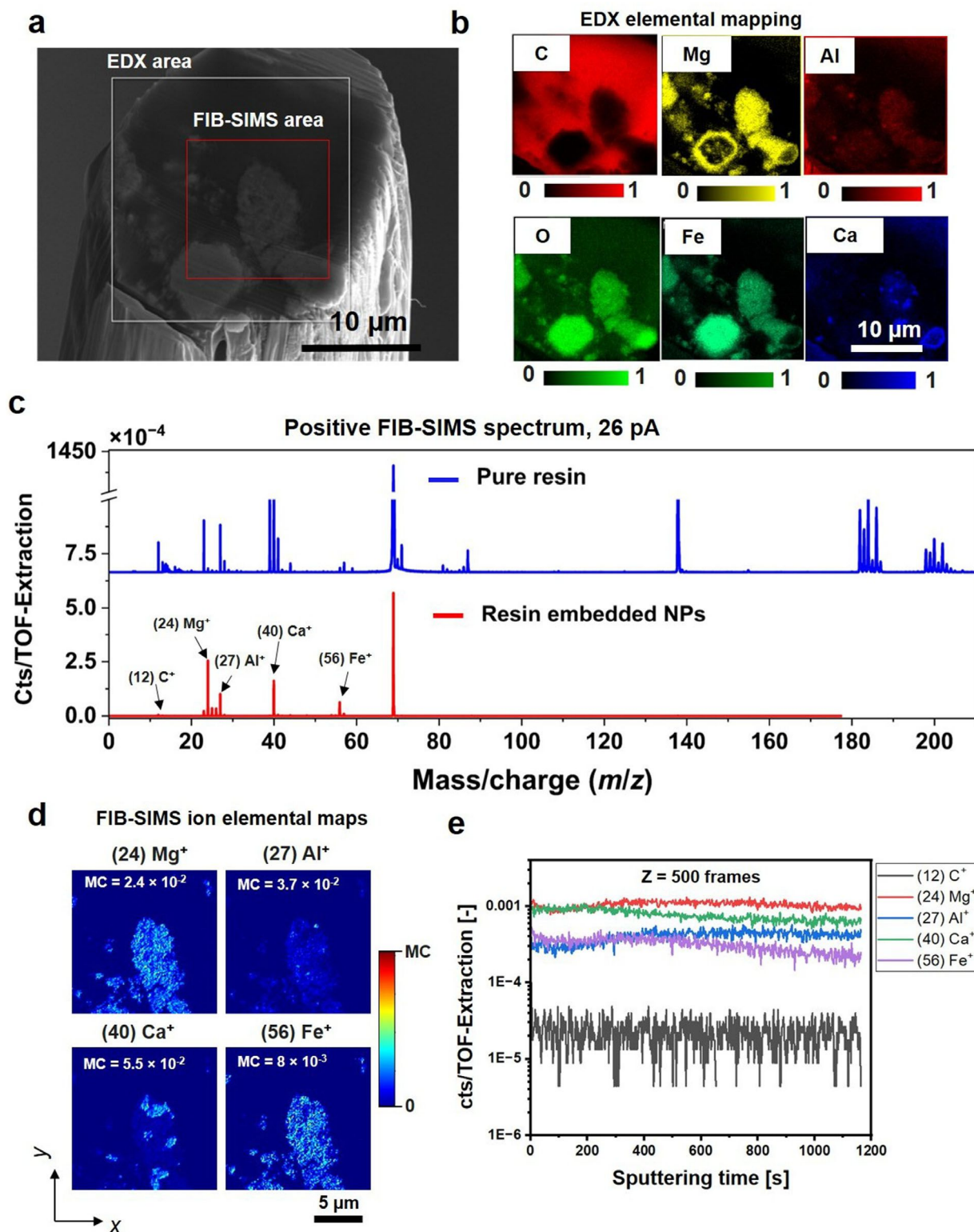


**Figure 4.** Correlative elemental mapping of resin-embedded catalyst NPs with EDX and FIB-SIMS: a) SEM overview of the FIB-exposed pillar surface with analyzed EDX ROI in the white box (20  $\mu\text{m} \times 20 \mu\text{m}$ ) and FIB-SIMS in the red box (15  $\mu\text{m} \times 15 \mu\text{m}$ ). b) EDX elemental mapping of C, O, Mg, Al, Fe, and Ca. c) SIMS spectra positive ions corresponding to pure resin (blue) and resin-embedded NPs (red). d) FIB-SIMS ions map in the x-y plane (top view) for (27)  $\text{Al}^+$ , (24)  $\text{Mg}^+$ , (40)  $\text{Ca}^+$ , and (56)  $\text{Fe}^+$ , with each pixel resolution of  $\approx 60 \text{ nm}$  representing the sum of intensities compiled over all frames. In the maps, the scale is such that the counts/TOF extraction per-pixel intensities vary from 0 to MC (the maximum counts). e) SIMS counts in the depth (z) direction.

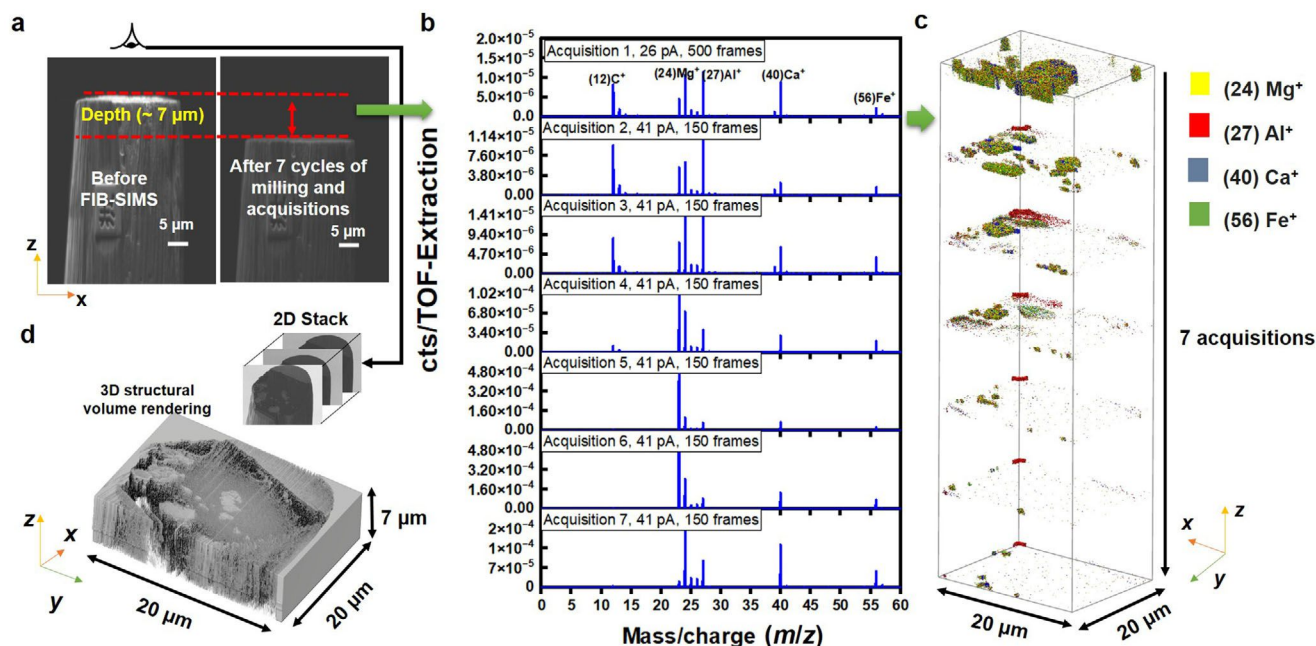


**Figure 5.** A series of FIB-SIMS acquisitions (7 cycles) on a micropillar for 3D analysis: a) x-z plane SEM images of the micropillar captured before and after the seven SIMS acquisitions with an  $\approx 7 \mu\text{m}$  milled depth (including both FIB slicing and FIB-SIMS imaging) in the z-direction. (b) The overall SIMS mass spectrum. c) 3D reconstruction of each SIMS acquisition. For display purposes, the data is rendered in  $(15 \mu\text{m} \times 15 \mu\text{m} \times 70 \mu\text{m})$  volume, with spacing of  $10 \mu\text{m}$  between SIMS acquisitions and colors for isotopes chosen for visualization. d) 3D volume rendering of FIB-slice and view.

in one instrument.<sup>[26]</sup> Bright Field (BF) and high-angle annular dark field (HAADF) STEM images were acquired at varying electron doses. An electron dose range of  $326.10\text{--}1543 \text{ e} \text{ \AA}^{-2} \text{ V}$  ( $70 \text{ pA}$ ,  $8.49\text{--}20.1 \text{ \AA}^2$ ,  $30 \mu\text{s}$ ) was sufficient to distinguish and analyze individual NPs from the resin matrix.

Figure 6b shows a BF STEM image of the entire membrane, obtained at an electron dose of  $0.2 \text{ e} \text{ \AA}^{-2}$ , revealing irregular NP/cluster distribution and detailed views of the NPs dispersed within the resin film. Magnified STEM images in Figure 6c,d acquired at a dose of  $1543 \text{ e} \text{ \AA}^{-2}$  (typically  $30 \text{ keV}$ ,  $70 \text{ pA}$ ,  $8.5 \text{ \AA}^2$ ,  $30 \mu\text{s}$ ) typically showed near-spherical shaped particles with diameters between  $30$  and  $44 \text{ nm}$  in perfect agreement with,<sup>[23]</sup> but frequently formed clusters up to  $\approx 175 \text{ nm}$  in size. The resin remained stable under the above conditions, and no charging effect was observed. However, at doses higher than  $1543 \text{ e} \text{ \AA}^{-2}$ , noticeable damage to the resin film resulted, as shown in Figure 6e.

### 2.3.4. Atom Probe Tomography of Resin-Embedded Catalyst NPs

The as-fabricated resin APT nanoneedles (Figure 3c, Figure S4, Supporting Information) were utilized for APT analysis due to their suitability for the technique. Figure 7a presents the analyzed APT specimen, which is comprised of particle regions and resin regions. This specimen was analyzed by APT but underwent several fractures through the course of the experiment, so different phase-pure regions have been analyzed separately. Figure 7b shows mass spectra from regions corresponding to resin and a  $\text{MgFe}_2\text{O}_4$  spinel NP.<sup>[23]</sup> Prominent peaks in the spectrum have been identified and labeled using insights from EDX-SIMS analy-

sis and reference data,<sup>[23]</sup> with their decomposition listed in Table S4, Supporting Information. Reconstructed positions of selected ions are shown in Figure 7c for the particle and Figure 7d for the resin, with both showing approximately homogenous distributions of the ranged ions.

The main peaks in the resin mass spectrum are at  $1 \text{ Da}$  (ranged as  $\text{H}^+$ , though the specimen H content cannot be distinguished from residual  $\text{H}_2$  in the chamber),<sup>[27]</sup>  $6 \text{ Da}$  and  $12 \text{ Da}$  ( $\text{C}^{++}$ ,  $\text{C}^+$ ),  $26 \text{ Da}$  ( $\text{CO}^+$ ) and  $44 \text{ Da}$  ( $\text{CO}_2^+$ ). The main peaks from the particle region are at  $12 \text{ Da}$  ( $\text{Mg}^{++}$ ),  $16 \text{ Da}$  ( $\text{O}^+$ ),  $26 \text{ Da}$  ( $\text{Fe}^{++}$ ),  $32 \text{ Da}$  ( $\text{O}_2^+$ ), and  $72 \text{ Da}$  ( $\text{FeO}^+$ ). The absence of  $\text{C}^+$  in the particle mass spectrum suggests the absence of  $\text{C}^+$ , supporting the assignment of the  $12 \text{ Da}$  peak as  $\text{Mg}^{++}$ . All peaks, but particularly  $\text{Mg}^{++}$ , show dramatic thermal tails which complicate compositional analysis. Inspection of the multiple histograms<sup>[28]</sup> shows these thermal tails are most likely the result of DC evaporation resulting from an excessively warm specimen apex. The background-corrected decomposed atomic composition of the particle, based on the ranged ions in Figure 7b, is  $15.2 \pm 0.1 \text{ at.\% Mg}$ ,  $44.2 \pm 0.2 \text{ at.\% Fe}$ ,  $40.2 \pm 0.2 \text{ at.\% O}$ , and  $0.43 \pm 0.05 \text{ at.\% Al}$ . The underestimation of O content from semiconductors is common in APT,<sup>[29]</sup> and putting that aside, the Mg:Fe:Al ratio is  $\approx 25:74:0.7$ , compared to the expected values of  $33:60:7$  based on the reported stoichiometry.<sup>[23,30]</sup> The strong thermal tail following  $\text{Mg}^{++}$  most likely comprises Mg ions, which explains the apparent underestimation of the Mg content. This strong thermal tail also includes the  $\text{Al}^{++}$  peak at  $13.5 \text{ Da}$ , which may impact the accurate quantification of Al content. Importantly, no significant Ga ions were detected, further supporting the chemical integrity of the NPs during FIB preparation.

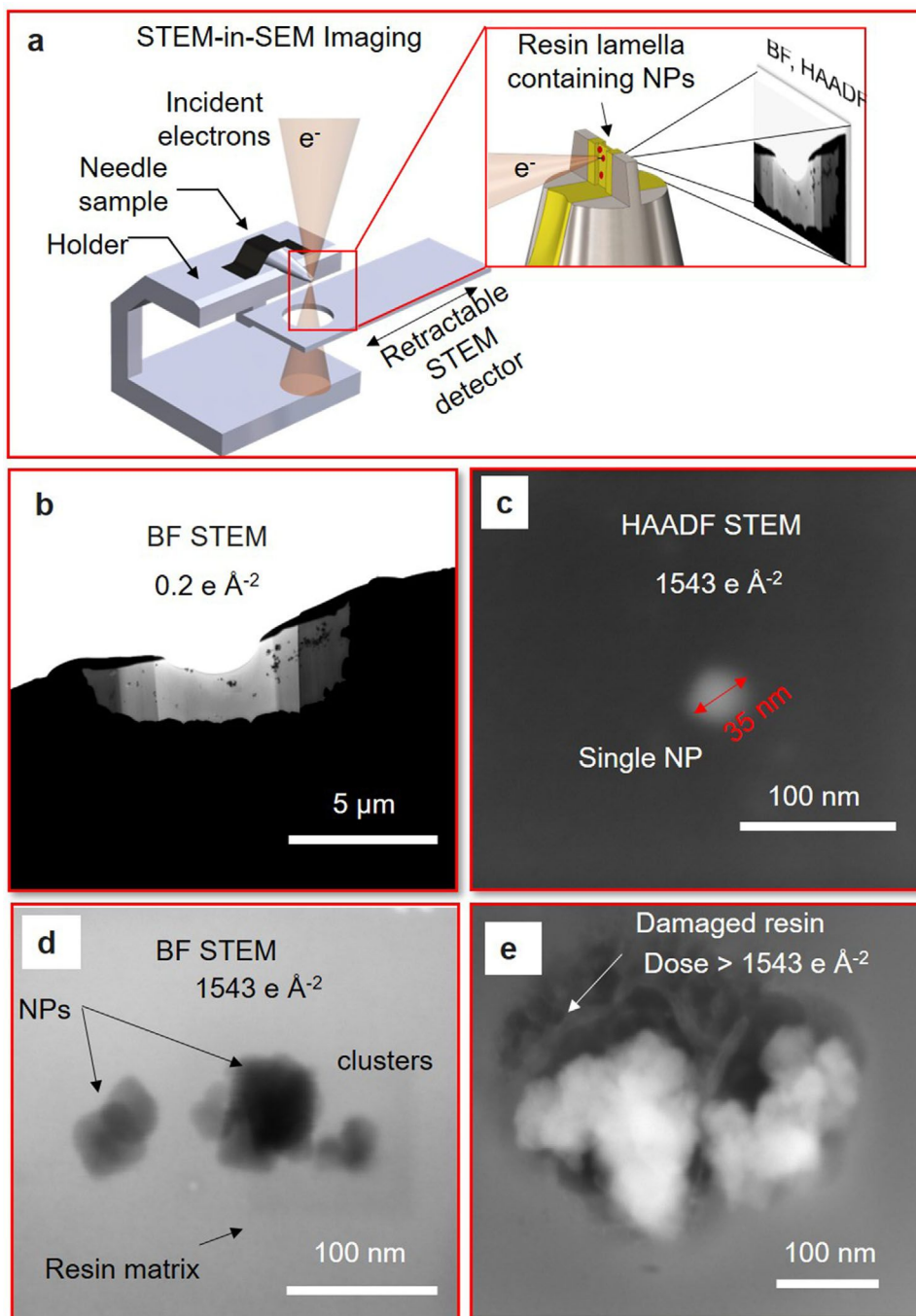


**Figure 6.** STEM analysis of resin-embedded NPs prepared in lamella geometry: a) Schematic representation of the experiment showing the needle position to the electron beam. b) BF STEM image of the entire lamella, in which the dark spots correspond to the embedded catalyst NPs. Electron irradiation was maintained at a consistent exposure dose of  $0.2 \text{ e } \text{\AA}^{-2}$ . c) Magnified HAADF STEM image of an individual NP ( $\approx 35 \text{ nm}$ ) obtained at the dose of  $1543 \text{ e } \text{\AA}^{-2}$ . d) BF STEM image of overlapped NPs and clusters. e) HAADF BF image illustrating damage to the sample due to excessive electron dose ( $>1543 \text{ e } \text{\AA}^{-2}$ ).

The decomposed atomic composition of the resin region is  $25.2 \pm 0.1 \text{ at.}\% \text{ H}$  (although this contains contributions from the residual  $\text{H}_2$  in the chamber),  $45.9 \pm 0.1 \text{ at.}\% \text{ C}$ , and  $28.8 \pm 0.1 \text{ at.}\% \text{ O}$ , although DC evaporation also causes strong thermal tails, which complicate analysis.

### 3. Discussion

The results presented above collectively demonstrate the potential of the proposed NEM method as a promising sample preparation method for NPs. The capillary-driven microchannel filling

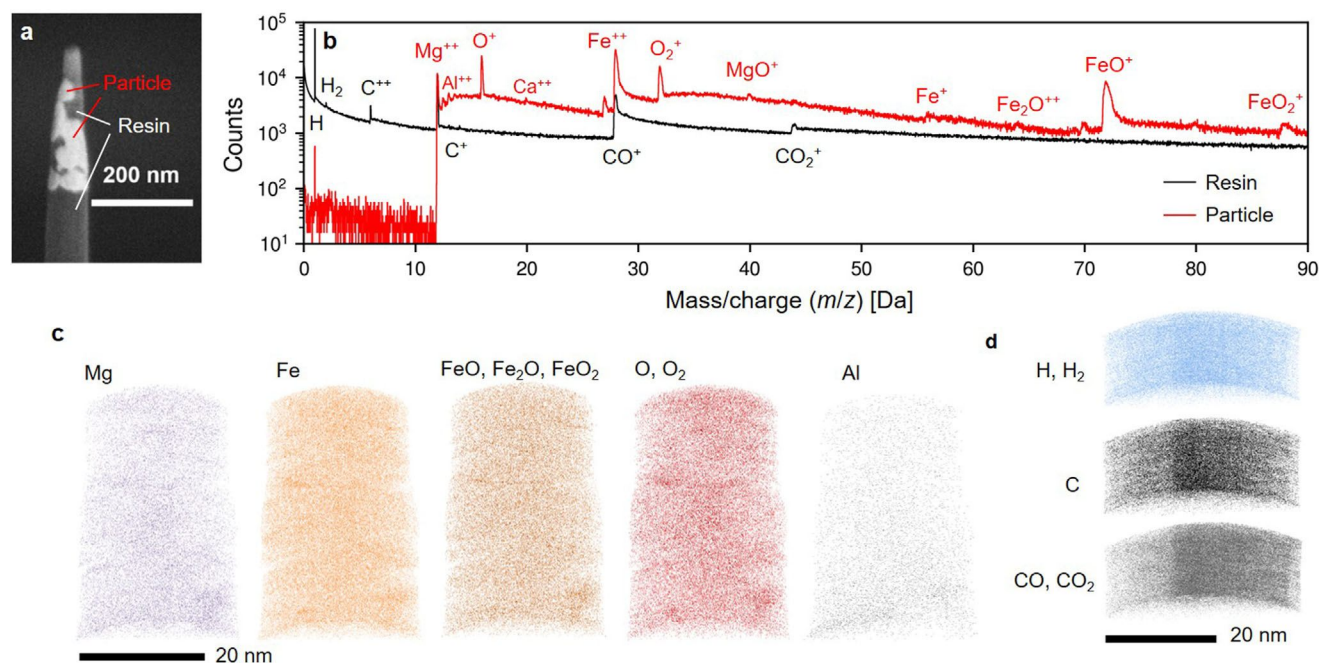


**Figure 7.** APT analysis of catalyst NPs embedded in resin. a) SEM image of the analyzed specimen prepared using FIB annular milling, with the resin and particles labeled. b) APT mass spectra from the resin region and the particle region. Selected ranged peaks are labeled. c) Reconstructed positions of key ions from the particle region of the data. d) Reconstructed positions of all ions from the resin region of the data.

provided a rapid, straightforward approach for retaining a picoliter volume of catalyst NPs (30–175 nm) dispersed in a resin precursor within the needle-eye, which is then polymerized in situ. A key advantage of this study is that each trapped specimen is verified by optical microscopy before polymerization, which increases effectiveness of the trapping process. Polymerization on multiple separate needles (Figure S1, Supporting Information) under identical experimental conditions demonstrated the reproducibility of our approach.

The metallic nature of the NPs used in this work facilitated their straightforward identification due to their higher atomic weight, which provided strong contrast in SEM imaging relative to the surrounding resin matrix. This contrast facilitated the rapid selection of ROIs for targeted FIB milling. In cases where NPs lack sufficient SEM contrast, complementary techniques such as EDX or FIB-SIMS can be employed to locate the ROIs and guide subsequent FIB milling.<sup>[31]</sup> Our FIB milling strategies on the needle tip included producing (1) H-bar for lamella preparation, (2) annular milling for single micropillar and ATP tip fabrication, and (3) tip array milling for multiple APT tips. All these geometries proved to be suitable for 3D FIB-SIMS, (S)TEM, and APT, eliminating the need for time-consuming and skill-demanding traditional FIB lift-out.

Moreover, comprehensive structural and chemical characterization of catalyst NPs was achieved using our method. In terms of structural analysis, STEM-in-SEM imaging of the resin-embedded NPs lamella and APT tips (Figure 6, Figure S4, Supporting Information) demonstrated excellent sample stability and enabled measurement of NP size, morphology, and distribution, both individually and in clusters. The same specimens are amenable to atomic-resolution TEM for further investigation

at higher resolution of crystallinity and lattice defects, thereby revealing any sample preparation-induced artefacts. Furthermore, 3D morphology of the NPs within the lamella can be reconstructed by electron tomography with tilt series acquisitions up to 120°;<sup>[4,17]</sup> and compositional heterogeneities can be mapped through correlative APT-TEM analysis on the APT tips. Selection of ROI on the lamella (Figure 6b) and fabrication of APT tips from electron-transparent lamellae can also be achieved following the protocol described in a previous work.<sup>[32]</sup>

In terms of chemical composition, FIB-SIMS ion maps of the major metallic elements in the NPs showed a strong correlation with EDX elemental maps (Figure 4), confirming consistent detection across both techniques. The primary  $\text{Ga}^+$  ion doses  $0.81\text{--}8.38 \times 10^{16}$  ions per frame (calculated from a  $225\text{--}400 \mu\text{m}^2$  field-of-view at  $256 \times 256$  pixels,  $\approx 60 \text{ nm pixel}^{-1}$ ) yielded sufficient secondary-ion counts to detect Mg, Al, Fe, and Ca from the clusters. This could be improved to achieve individual NP resolution by lowering the beam current, selecting a matrix with more favorable ion-yield characteristics, or modifying the surface chemistry prior to analysis by oxygen to enhance ion yields, as demonstrated in previous studies.<sup>[5,33]</sup> Isotopic and oxide assignments were ambiguous due to interferences from multiple molecular ions from the NPs and the resin. For instance, the isotope abundance of Fe deviates from natural isotope abundance (i.e.,  $^{54}\text{Fe}$  (5.8%),  $^{56}\text{Fe}$  (91.7%), and  $^{57}\text{Fe}$  (2.2%)), meaning that the  $m/z = 56$  peak tentatively assigned to  $\text{Fe}^+$ , may include signals from  $\text{CaO}^+$ , and  $\text{MgO}_2^+$ . Similarly, the secondary ion at  $m/z = 40$  peak assigned to  $\text{Ca}^+$ , likely also interferes with  $\text{MgO}^+$ , resulting in ambiguity in peak assignment. We detected some metal oxides ( $\text{FeO}$ ,  $\text{FeO}_2$ , and  $\text{AlO}$ )<sup>[23]</sup>, but others such as  $\text{Fe}_2\text{O}_3$  were absent, probably due to the positive secondary ion mode used and the

reduced efficiency of oxide ejection when using a 30 keV Ga<sup>+</sup> primary ion beam. Moreover, our needle-eye sample preparation proved suited for 3D FIB-SIMS methodology.<sup>[34]</sup>

In APT experiments, we achieved quantitative compositional analysis of the catalyst NPs with results closely approximating those reported before,<sup>[23]</sup> despite limitations. Four APT tips whose NP presence at the apex confirmed by (S)TEM were selected for analysis. Two tips yielded comparable field evaporation and produced mass spectra exceeding two million ions with clear NPs detection characteristics; while the other two fractured prematurely without any NP signature but still yielded at least 200 000 ions each. Fractures likely arose due to weak adhesion between the NPs and the resin under the high electric field and from the heterogeneous field-evaporation behavior of multi-component systems,<sup>[35]</sup> and also because no coating was applied on the samples. Similar to FIB-SIMS, peak identification in successful APT data was ambiguous due to interferences from multi-component in the NPs and the hydrocarbon and oxygen-containing ions from the matrix. Complex field evaporation behaviors in multi-component systems, including differential evaporation rates, molecular dissociation, and hydride formation, distorted the mass spectrum. Additionally, this caused sample fractures, which posed a significant limitation, affecting data quality and the success rate. Preparing a closely evaporation field-matched matrix material that fully surrounds the NPs or applying thin conductive coatings prior to analysis may improve the yield of our method.<sup>[19,36]</sup>

Next, we want to discuss potential improvements to the NEM preparation method. FIB milling was extensively used in this work to first create the microchannels and fabricate geometries. Despite our FIB milling strategies and parameters (Table S1, Supporting Information), we acknowledge that FIB-prepared specimens are not entirely free from any prior preparation-induced artifacts. Ga implantation and structural damage, particularly at the sample surface, remain inherent challenges. To mitigate this, implantation-free and faster fabrication techniques will be explored. We speculate that femtosecond laser ablation and plasma FIB, both of which offer higher removal rates and minimal ion contamination, could be explored.<sup>[16,37]</sup> Additionally, we observed structural damage of some of the needle tips during preparation, resulting in either bending or complete removal of the cap while polymerizing the specimen within the microchannel (Figure S7, Supporting Information). This proved advantageous, as it eliminated the need for extensive FIB milling to create a fresh surface on resin surface. This suggests that intentional fracture could be investigated as a time-saving strategy to further streamline the preparation. Future improvements will also focus on optimizing the microchannel dimensions to broaden the method's applicability across diverse nanomaterials and liquid specimens. We anticipate that vitrifying liquids on the needle tip for cryo-imaging and analysis will expand the applicability of the method to biological studies. Systematic studies on the relationship between liquid properties, needle substrate surface properties, and microchannel dimensions will elucidate filling dynamics, establish design rules, and help to achieve ever-smaller volumes down to the femtoliter-attoliter scales.

From a practical point of view, it should be mentioned that the W needle as substrate turned out to be well suited and mechanically stable in most of the experiments, especially when

immersing for confining the specimen, and also when transferring between analytical instruments. But other substrates can be adopted. In case of applicability to organic samples, further consideration is required. One potential concern is the biocompatibility of the needle substrate, which may pose compatibility issues for certain biological specimens. Alternative strategies will be considered in future work, such as coating the needles with gold (Au) or selecting biocompatible needle materials that provide both chemical stability and the mechanical durability required to withstand various preparation conditions without degradation or adverse reactions. Also, significant challenges arose when initial tests on biological samples, such as cells. Identifying cells within the exposed volume using FIB-SEM proved difficult due to their organic composition and low atomic contrast, making them visually indistinguishable from the surrounding resin in SEM imaging. This lack of contrast complicated the assessment of whether cells were successfully trapped within the microchannel or if the structure contained only the surrounding resin medium. Potential solutions to enhance visibility include staining or functionalizing the cell with electron-dense markers, such as heavy metal stains, to improve contrast and facilitate precise localization in SEM imaging.

#### 4. Conclusion

In this work, we presented a sample preparation method for the comprehensive analysis of NPs. We introduced a “needle-eye” design, featuring a through-microchannel at the needle tip that enables controlled trapping of resin precursors with suspended NPs via pressure-driven filling upon immersion in a liquid suspension. The retained specimen was then polymerized in situ on the needle tip for subsequent analysis. Using catalyst NPs as an application example, we demonstrated the applicability of this approach for room temperature analysis. Needle samples were prepared with polymerized volumes ranging from 6 to 60 pL, and subsequent FIB milling was employed to rapidly create specific geometries on the needle tip, such as a micropillar, a lamella, and APT tips. We showcased the use of EDX, FIB-SIMS, STEM, and APT techniques to analyze the chemical and structural properties of tiny NPs. Indeed, the combination of these techniques has been proven effective in the analysis of the NPs both correlatively and complementarily. The findings confirm the method's ability to preserve structural and chemical properties. Our method offers several key advantages: (1) precise sample capture with high repeatability and volume control in the picoliter range, (2) elimination of complex processing steps, including FIB lift-out, micro/nanomanipulation, and microtomy, (3) scalability for high-throughput analysis using multi-needle arrays, (4) reduced starting material requirements and preparation time, (5) site specific machining with compatibility for multimodal analysis combining both correlative and complementary investigations, (6) flexibility for both room-temperature and cryogenic analysis through vitrification. Future improvements include refining the method to target smaller nanoscale trapped volumes (from femtoliter to attoliter) by reducing channel sizes and applying surface treatments to enhance hydrophilicity, which will also reduce machining time. Addressing biocompatibility challenges for organic specimens and minimizing cluster formation in grid materials will further enhance the applicability of the method.

Despite these limitations, the NEM method remains an effective approach for sample preparation, offering the potential to overcome current bottlenecks in high-resolution nanomaterial analysis. While this study serves as a proof of concept, further investigation and optimization will be essential to fully consolidate the efficacy of the method.

## 5. Experimental Section

**Preparation of Suspensions—Pure Resin Precursor.** The uncatalyzed LR white liquid resin precursor (hard grade) used in this study was purchased from ProSiTech, Australia (Product CO24) and the kit was supplied with an initiator (benzoyl peroxide catalyst powder). The resin precursor was highly hydrophilic with a low viscosity of 8 cps. To prepare the resin suspension, 1 mL of precursor and 0.02 g of initiator were added to a microcentrifuge tube and ultrasonically mixed for 5 min to ensure uniform dispersion of the initiator. The mixture was then stored in a refrigerator at 4 °C to fully dissolve the initiator into the resin precursor, maintaining the mixture in a liquid state to prevent premature polymerization.

**Preparation of Suspensions- Catalyst Nanoparticles Dispersed in Resin Precursor.** In this study, Mg, Al, Ca, and Fe-rich multi-metallic catalyst NPs, primarily synthesized as spinel ferrite from fly ash waste from the decommissioned Yallourn coal power plant in Victoria, Australia were used to test the proposed NEM sample preparation method. A slightly modified NPs synthesis procedure previously reported by<sup>[30]</sup> was adopted. Initially, 1 kg of raw fly ash was washed in water several times to remove water-soluble materials (Na<sub>2</sub>O, K<sub>2</sub>O, etc.) and all unburnt carbon. The washed material was leached using 32% HCl acid solution with a liquid-to-solid (L/S) ratio of 10 under continuous stirring for 3 h. This purposely facilitates the extraction of significant amounts of Fe, Al, and Mg from the solid matrix. Subsequently, the leachate was titrated by adding 1 M NaOH until the pH reached 10. The precipitate was water-washed, mixed with glycine in a 1:1 ratio, and dried overnight to form a gel-like substance. The gel was then combusted at 800 °C for 4 h to form the NPs.

To prepare the resin-NPs suspension, the resin precursor was first mixed with the catalyst NPs at an 8 wt% ratio and ultrasonically mixed for 30 min to ensure even dispersion. Following this, the initiator was added, and the mixture was sonicated for an additional 5 min to achieve thorough dispersion. The suspension was then refrigerated at 4 °C to fully dissolve the initiator into the precursor and the mixture in a liquid state to prevent premature polymerization.

**Needle-Eye Microtrap based Sample Preparation—Needle-Eye (Through-Microchannel) Fabrication on Needle Tip:** A needle eye design featuring a through-microchannel was fabricated at the tip of a tungsten (W) needle substrate using FIB milling. W needles (ST-20-010 from GGB Industries, Inc.) with an initial tip radius of  $\approx 10 \mu\text{m}$  were selected for their mechanical hardness (Figure 2a). A rectangular pattern ( $w \times h$ ) was milled into the side of the needle using FIB milling (65 nA and 30 keV, FEI Quanta 3D, Thermo Fisher, USA).

**Needle Plasma Surface Modification:** After microchannel fabrication, the needle tip was cleaned by sequential immersion in ethanol and isopropanol, then subjected to a 5-min oxygen plasma surface modification to enhance surface hydrophilicity. The plasma cleaning was conducted using XEI Evactron Softclean Zephyr Plasma Cleaner.

**Needle Immersion in Suspension and Microchannel Filling:** The needle was immersed in the target liquid suspension (prepared suspensions in previous sections) held in a reservoir to fill the microchannel (Figure 1 (Step 2)). Initial trials used pure resin precursor, followed by experiments with NP-suspended resin precursor. After immersion, the reservoir was placed in a low vacuum chamber to help remove air bubbles. The needle was then retracted and examined under brightfield optical microscopy (Eclipse E200, Nikon, Tokyo, Japan). Images were collected under transmission and reflection modes using a digital camera (Pro-MicroScan 5898, Nikon, Tokyo, Japan). Upon confirmation, on-tip polymerization was performed.

**On-Tip Polymerization:** A temperature of 70 °C was set in the vacuum oven (VO Series 500°F Vacuum Drying Oven) to initiate polymerization

of the resin suspension within the microchannel. Since resin retention was confirmed via optical microscopy pre-checks, the needle could be directly placed in the vacuum oven for polymerization. However, to minimize evaporation of the retained specimen over time, the needles were preferably kept immersed in the resin-based suspension, and the entire setup (including the reservoir) was placed in the oven (at 84 659.7 Pa). After 5 min of partial polymerization, the needles were carefully removed from the hardened resin block, resulting in a partially solidified specimen within the microchannel. The removed needles were then left to fully polymerize for 24 h before subsequent electron microscopy (EM) imaging in the FIB/SEM system.

**Scanning Electron Microscopy Imaging and chemical Characterization:** The FIB/SEM instrument (FEI Quanta 3D, Thermo Fisher, USA) was used to examine the samples including as-received NPs, needles, and on-tip polymerized specimen. SEM imaging was employed for morphology and size information, while the instrument's EDX detector was used to examine the chemical composition. SEM imaging was performed using accelerating voltage kept between 2–5 keV and 10–50 pA to minimize electron beam damage and avoid charging effects. The instrument's Ga<sup>+</sup> FIB column was used for milling.

**FIB Milling Geometries (Micropillar, Lamella and APT Tip) Fabrication on Needle Tip:** FIB milling was used to create the geometries using the parameters summarized in Table S1, Supporting Information.

**Resin-embedded NPs lamella fabrication:** The well-established H-bar approach was used for the preparation of electron transparent (lamella) geometry.<sup>[38]</sup> As illustrated in Figure S2, Supporting Information, a ROI on the freshly FIB-exposed resin-embedded NPs surface was identified using SEM-EDX. A protective Pt layer was then deposited (yellow rectangle) over the ROI, and deep trenches were milled from both sides the Pt-capped ROI along the long edges (the red semi-circles) to create the H-bar. Final thinning at a low energy FIB milling using a 5 keV Ga<sup>+</sup> was introduced to reduce the amount of damage and amorphization introduced during the preceding 30 keV milling step.

**Resin-embedded NPs micropillar and APT tips fabrication:** FIB annular milling was performed at 30 keV to fabricate a fine micropillar with a 30  $\mu\text{m}$  inner diameter and an aspect ratio of 0.9:1. The probe current was reduced in steps from 15 nA to 9.9 nA and then to 4 nA, while the ion beam was rastered from outer to inner scan direction to minimize redeposition.

Figure S3, Supporting Information presents the sequential steps used to fabricate a resin ATP tip. In the first step a capping layer was deposited on the ROI using e-beam-induced (100 nm) followed by ion-beam-induced (300 nm) deposition, giving a capping of  $\approx 400 \text{ nm}$  thick and 3–4  $\mu\text{m}$  in diameter. Annular FIB milling was then employed to give the resin-embedded NP a tip shape with the required dimension (an apex radius  $< 100 \text{ nm}$ ). Finally, a 10 s low energy polish (5 keV, 41 pA broad beam) was used.

In an effort to ensure that at least one APT tip provides high-quality APT dataset, we adopted a tip array strategy. Four sharp APT tips were milled  $\approx 10 \mu\text{m}$  apart on a single on-tip polymerized specimen (Figure S4a, Supporting Information). STEM screening confirmed NPs positioned at the apex of three of the four tips (Figure S4b, Supporting Information). However, the APT electrode detectors' field of view did not allow for the analysis of all four tips from one needle, as running one placed the others in the detector's field of view, likely representing secondary peaks in the mass spectrum. Only one tip was selected for APT, while the others were blunt (Figure S4c, Supporting Information). This suggests that redesigning the microchannel to provide a spacing of  $\approx 40 \mu\text{m}$  between sharpened APT tips could allow for two or more usable tips per needle, offering a potential high-throughput option. Throughput can also be increased by polymerizing specimens on several needles in parallel and then FIB-sharpening each one.

STEM inspection revealed NP-rich regions along the APT needle shank. If a tip fractured during APT analysis, FIB was used to re-sharpen the needle at another region containing NPs, allowing for a new analysis to be conducted (Figure S4c, Supporting Information). This iterative FIB re-sharpening approach proved highly valuable in this study.

**FIB damage mitigation:** Since FIB milling leads to a certain level of structural and compositional damage,<sup>[39]</sup> to ensure quality and integrity

of the prepared geometries following strategies were used: the resin surface was kept parallel to the ion beam during surface polishing at 30 keV. It has been observed that milling at an incidence angle of 89° between the ion beam and a vector normal to the resin specimen surface leads to  $5.2 \pm 3.4$  nm Ga<sup>+</sup> implantation and the amorphization of the outer layer, a final FIB milling at 2 keV with a current of 29 pA was used to reduce the thickness of the damaged surface to  $1.4 \pm 0.9$  nm depth.<sup>[40]</sup> On the other hand, when creating geometries, the sample surface was positioned perpendicular to the ion beam. Milling at 30 keV perpendicular to a resin sample surface results in  $\approx 42$  nm Ga<sup>+</sup> implantation depth. Reducing the ion voltage to 2 keV can reduce ion implantation as low as  $\approx 7.6$  nm depth. However, because a protective  $>400$  nm Pt layer was maintained on the resin surface before geometry (lamella and APT tip) fabrication, Ga<sup>+</sup> implantation on the top surface may not be a concern in our milling strategy. Nonetheless, lateral Ga<sup>+</sup> implantation in the walls of the geometries during the fabrication process can be estimated to be high  $\approx 10$  nm as well as heat damage. To reduce the effects of beam heating, one set up the milling parameters such that the overlap between the subsequent milling spots was within the outer ranges of the beam straggle. This approach was demonstrated before to create clean cross-sections with reduced heat damage, even when employing a high-current milling strategy.<sup>[41]</sup>

**FIB-SIMS:** FIB secondary ion imaging was conducted using a vacuum-compatible, high-resolution ToF-SIMS detector from TOFWERK (Thun, Switzerland), integrated within the Thermo Scientific Helios 5 UX FIB/SEM system. The system's Ga<sup>+</sup> FIB column was used to mill the ROI. During SIMS imaging, secondary positively and negatively charged single ions and ionized fragments are generated and guided to a mass analyzer for mass analysis and therefore be detected. The extraction voltage for the secondary ions applied to the extraction nozzle of the ToF-SIMS was limited to  $< 200$  V, with the needle sample grounded, and a working distance kept at 4.1 mm. A FIB raster scan strategy was used and this study primarily focused on the collection of positive secondary ions for their higher ionization efficiency with metallic particles, providing stronger signals. SIMS data were collected according to the experimental parameters listed in Table S5, Supporting Information, utilizing different areas and beam currents for each sample. The mass spectra data and ion maps were processed using ToF SIMS Explorer, the built-in proprietary software.

Needle samples were mounted on a pre-tilted holder (45°) to facilitate transitions between the needle's axis being colinear and perpendicular to the ion beam for SIMS acquisitions and FIB slicing, as illustrated in Figure S8, Supporting Information. For SIMS acquisition, the configuration in Figure S8a, Supporting Information was used, followed by a 180° stage rotation and a  $-7^\circ$  tilt to align the ion beam parallel to the sample surface (Figure S8b, Supporting Information) for FIB slicing. Top-view (*x-y* plane) SEM images were acquired using the Everhart-Thornley Detector (ETD, secondary electrons) before each SIMS acquisition, with the electron beam set to 5 keV. Precise slice removal was automated using Thermo Fisher ASV software, while stage moving to SIMS acquisition was manually controlled. Slicing was performed with a 30 keV Ga<sup>+</sup> ion beam at a 9 nA probe current, removing  $\approx 1$  μm of material to expose a fresh surface for the next SIMS acquisition.

This method enabled seven FIB-SIMS acquisitions for depth profile analysis. Serial SIMS acquisitions and FIB/SEM slice-and-view images allowed for 3D reconstruction of the internal structure and chemistry of the samples. FIB/SEM stacks were visualized and processed in AVIZO 2021.2, and 3D rendering of SIMS ion distributions was achieved using a custom MATLAB script.

**STEM Structural Analysis of Resin-Embedded Nanoparticles Lamella and APT Tips:** STEM-in-SEM imaging was performed using a FEI Quanta 3D FEGSEM (Thermo Fisher, USA) equipped with a retractable STEM detector. The holder was mounted on the SEM stage, with the needles mounted using carbon tape while their tips remained suspended (Figure 6a). The STEM detector was then inserted beneath the suspended needle tip and aligned to ensure the electron beam penetrates the lamella/APT tip and reaches the detector. Typical STEM-in-SEM operating conditions included

a 30 keV acceleration voltage,  $\approx 70$  pA probe current, and a 10 mm working distance.

**APT Characterization:** APT was performed using a local-electrode atom probe (LEAP) 4000X-Si to analyze the prepared specimens. Field evaporation was conducted in laser-pulsed mode with a wavelength ( $\lambda$ ) of 355 nm. The pulse frequency was set to 200 kHz, with a pulse energy of 50 pJ and a sample temperature of 50 K. The detection rate during the analysis was maintained at 0.5% (0.005 ions per pulse). Data reconstruction was carried out using IVAS software version 3.6.8 (Cameca Scientific Instruments), following a standard voltage evolution-based protocol with varied reconstruction factors to ensure accurate spatial and compositional analysis.

## Supporting Information

Supporting Information is available from the Wiley Online Library or from the author.

## Acknowledgements

This study was partially funded by the Australian Research Council (LP220100365). The authors acknowledge the use of the instruments and scientific and technical assistance at the Monash Centre for Electron Microscopy (MCEM), Monash University, a Microscopy Australia (ROR: 042mm0k03) facility supported by NCRIS. This research used equipment funded by Australian Research Council grants (LE200100132, LE0882821). The authors also acknowledge the technical and scientific assistance of Sydney Microscopy & Microanalysis (SMM), the University of Sydney Node of Microscopy Australia. This work was also performed in part at the Melbourne Centre for Nanofabrication (MCN) in the Victorian Node of the Australian National Fabrication Facility (ANFF).

Open access publishing facilitated by Monash University, as part of the Wiley - Monash University agreement via the Council of Australian University Librarians.

## Conflict of Interest

The authors declare no conflict of interest.

## Data Availability Statement

The data that support the findings of this study are available from the corresponding author upon reasonable request.

## Keywords

mixed metal oxide catalyst, multimodal and correlative microscopy, nanoparticles, needle-eye design, on-tip polymerization

Received: March 31, 2025  
Revised: May 3, 2025  
Published online: May 26, 2025

- [1] a) X. Han, K. Xu, O. Taratula, K. Farsad, *Nanoscale* **2019**, *11*, 799; b) Y. Dai, J. Ju, L. Luo, H. Jiang, Y. Hu, C. Li, *Small Methods* **2024**, *8*, 2301768; c) M. J. Mitchell, M. M. Billingsley, R. M. Haley, M. E. Wechsler, N. A. Peppas, R. Langer, *Nat. Rev. Drug Discovery* **2021**, *20*, 101; d) J. Singh, T. Dutta, K.-H. Kim, M. Rawat, P. Samddar, P. Kumar, *J. Nanobiotechnol.* **2018**, *16*, 84.

- [2] N. Joudeh, D. Linke, *J. Nanobiotechnol.* **2022**, *20*, 262.
- [3] C. Jiang, S. Liu, T. Zhang, Q. Liu, P. J. Alvarez, W. Chen, *Environ. Sci. Technol.* **2022**, *56*, 7426.
- [4] a) O. Guise, C. Strom, N. Preschilla, *Polymer* **2011**, *52*, 1278; b) C. Berger, N. Premaraj, R. B. Ravelli, K. Knoops, C. López-Iglesias, P. J. Peters, *Nat. Methods* **2023**, *20*, 499; c) H. Jinnai, X. Jiang, *Curr. Opin. Solid State Mater. Sci.* **2013**, *17*, 135; d) R. Leary, P. A. Midgley, J. M. Thomas, *Acc. Chem. Res.* **2012**, *45*, 1782; e) T. Rodenas, G. Prieto, *Catal. Today* **2022**, *405*, 2.
- [5] a) A. Römpp, B. Spengler, *Histochem. Cell Biol.* **2013**, *139*, 759; b) A. Priebe, J.-P. Barnes, T. E. J. Edwards, L. Pethö, I. Balogh, J. Michler, *Anal. Chem.* **2019**, *91*, 11834; c) J. Nuñez, R. Renslow, J. B. Cliff, C. R. Anderton, *Biointerphases* **2017**, *13*, 03B301.
- [6] P. Trzaskoma, B. Ruszczycki, B. Lee, K. Pels, K. Krawczyk, G. Bokota, A. Szczepankiewicz, J. Aaron, A. Walczak, M. Śliwińska, S41467-020-15987-2. | PubMed | ISI, **2020**, *11*, 2120.
- [7] a) T. F. Kelly, M. K. Miller, *Rev. Sci. Instrum.* **2007**, *78*, 031101; b) B. Gault, A. Chiamonti, O. Cojocar-Mirédin, P. Stender, R. Dubosq, C. Freysoldt, S. K. Mäkinen, T. Li, M. Moody, J. M. Cairney, *Nat. Rev. Methods Primers* **2021**, *1*, 51.
- [8] H. Zschiesche, A. P. C. Campos, C. Dominici, L. Roussel, A. Charai, D. Mangelinck, C. Alfonso, *Ultramicroscopy* **2019**, *206*, 112807.
- [9] N. B. Ghomrasni, C. Chivas-Joly, L. Devoille, J.-F. Hochepped, N. Feltin, *Powder Technol.* **2020**, *359*, 226.
- [10] C. Hacker, J. Asadi, C. Pliotas, S. Ferguson, L. Sherry, P. Marius, J. Tello, D. Jackson, J. Naismith, J. M. Lucocq, *Sci. Rep.* **2016**, *6*, 25275.
- [11] a) G. Eriksson, M. Hulander, M. Thuvander, M. Andersson, *Microsc. Microanal.* **2024**, *30*, 1036; b) J. E. Halpin, R. W. H. Webster, H. Gardner, M. P. Moody, P. A. J. Bagot, D. A. MacLaren, *Ultramicroscopy* **2019**, *202*, 121; c) E. V. Woods, M. P. Singh, S.-H. Kim, T. M. Schwarz, J. O. Douglas, A. A. El-Zoka, F. Giuliani, B. Gault, *Microsc. Microanal.* **2023**, *29*, 1992; d) Q. Yang, D. Joyce, S. Saranu, G. Hughes, A. Varambhia, M. Moody, P. Bagot, *Catal. Struct. React.* **2015**, *1*, 125; e) V. R. Adineh, R. K. Marceau, Y. Chen, K. J. Si, T. Velkov, W. Cheng, J. Li, J. Fu, *Ultramicroscopy* **2017**, *181*, 150.
- [12] a) D. J. Larson, A. D. Giddings, Y. Wu, M. A. Verheijen, T. J. Prosa, F. Roozeboom, K. P. Rice, W. M. M. Kessels, B. P. Geiser, T. F. Kelly, *Ultramicroscopy* **2015**, *159*, 420; b) D. E. Perea, J. Liu, J. Bertrand, Q. Dicken, S. T. Thevuthasan, N. D. Browning, J. E. Evans, *Sci. Rep.* **2016**, *6*, 22321; c) D. S. Mosiman, Y. S. Chen, L. Yang, B. Hawke, S. P. Ringer, B. J. Mariñas, J. M. Cairney, *Small Methods* **2021**, *5*, 2000692; d) F. Zand, S. J. T. Hangx, C. J. Spiers, P. J. van den Brink, J. Burns, M. G. Boebinger, J. D. Poplawsky, M. Monai, B. M. Weckhuysen, *J. Am. Chem. Soc.* **2023**, *145*, 17299; e) T. Pingel, M. Skoglundh, H. Grönbeck, E. Olsson, *J. Microsc.* **2015**, *260*, 125; f) V. R. Adineh, C. Zheng, Q. Zhang, R. K. Marceau, B. Liu, Y. Chen, K. J. Si, M. Weyland, T. Velkov, W. Cheng, *Adv. Funct. Mater.* **2018**, *28*, 1801439.
- [13] A. M. Schrand, J. J. Schlager, L. Dai, S. M. Hussain, *Nat. Protoc.* **2010**, *5*, 744.
- [14] a) P. L. Stewart, *Wiley Interdiscip. Rev. Nanomed. Nanobiotechnol.* **2017**, *9*, 1417; b) L. Tonggu, L. Wang, *Ultramicroscopy* **2020**, *208*, 112849; c) D. M. Long, M. K. Singh, K. A. Small, J. Watt, *Nanotechnology* **2022**, *33*, 503001; d) M. Marko, C. Hsieh, R. Schalek, J. Frank, C. Mannella, *Nat. Methods* **2007**, *4*, 215; e) M. Gao, Y. K. Kim, C. Zhang, V. Borshch, S. Zhou, H. S. Park, A. Jákli, O. D. Lavrentovich, M. G. Tamba, A. Kohlmeier, *Microsc. Res. Tech.* **2014**, *77*, 754; f) Y.-S. Chen, M. J. Griffith, J. M. Cairney, *Nano Today* **2021**, *37*, 101107; g) D. Schreiber, D. Perea, J. Ryan, J. Evans, J. Vienna, *Ultramicroscopy* **2018**, *194*, 89.
- [15] X. Jiao, L. Roiban, G. Foray, K. Masenelli-Varlot, *Micron* **2019**, *117*, 60.
- [16] a) M. Tkadletz, M. Schiester, H. Waldl, G. Schusser, M. Krause, *Mater. Today Commun.* **2024**, *39*, 108672; b) A. Sharma, S. Zhang, J. Fu, D. Marla, *Ultramicroscopy* **2024**, *265*, 114009; c) N. White, K. Eder, J. Byrnes, J. M. Cairney, I. E. McCarroll, *Ultramicroscopy* **2021**, *220*, 113161; d) M. Tkadletz, H. Waldl, M. Schiester, A. Lechner, G. Schusser, M. Krause, N. Schalk, *Ultramicroscopy* **2023**, *246*, 113672.
- [17] a) J. P. Josten, P. J. Felfer, *Microsc. Microanal.* **2022**, *28*, 1188; b) T. Przybilla, B. A. Zubiri, A. M. Beltrán, B. Butz, A. G. Machoke, A. Inayat, M. Distaso, W. Peukert, W. Schwieger, E. Spiecker, *Small Methods* **2018**, *2*, 1700276; c) A. Djoulde, T. L. Mamela, W. Su, L. Kong, H. Wang, J. Chen, J. Rao, P. Zhao, L. Ma, J. Yang, *ACS Appl. Nano Mater.* **2022**, *5*, 1110.
- [18] a) P. Felfer, T. Li, K. Eder, H. Galinski, A. P. Magyar, D. C. Bell, G. D. W. Smith, N. Kruse, S. P. Ringer, J. M. Cairney, *Ultramicroscopy* **2015**, *159*, 413; b) S.-H. Kim, P. W. Kang, O. O. Park, J.-B. Seol, J.-P. Ahn, J. Y. Lee, P.-P. Choi, *Ultramicroscopy* **2018**, *190*, 30.
- [19] a) S. Qiu, V. Garg, S. Zhang, Y. Chen, J. Li, A. Taylor, R. K. Marceau, J. Fu, *Ultramicroscopy* **2020**, *216*, 113036; b) S. Qiu, C. Zheng, Q. Zhou, D. Dong, Q. Shi, V. Garg, W. Cheng, R. K. W. Marceau, G. Sha, J. Fu, *J. Phys. Chem. C* **2020**, *124*, 19389.
- [20] a) S. Zhang, G. Gervinskis, S. Qiu, H. Venugopal, R. K. Marceau, A. De Marco, J. Li, J. Fu, *Nano Lett.* **2022**, *22*, 6501; b) L. Tegg, I. E. McCarroll, S.-H. Kim, R. Dubosq, E. V. Woods, A. A. El-Zoka, B. Gault, J. M. Cairney, *Microsc. Microanal.* **2024**, *30*, 1195; c) P. Azizian, J. Casals-Terré, J. Ricart, J. M. Cabot, *Analyst* **2023**, *148*, 2657; d) L. N. Acquaroli, R. Urteaga, C. L. Berli, R. R. Koropecski, *Langmuir* **2011**, *27*, 2067; e) A. Olanrewaju, M. Beaugrand, M. Yafia, D. Juncker, *Lab Chip* **2018**, *18*, 2323; f) F. F. Ouali, G. McHale, H. Javed, C. Trabi, N. J. Shirtcliffe, M. I. Newton, *Microfluid. Nanofluid.* **2013**, *15*, 309.
- [21] T. Ge, W. Hu, Z. Zhang, X. He, L. Wang, X. Han, Z. Dai, *Materials Today Bio* **2024**, *26*, 101048.
- [22] P. Koliopoulos, K. S. Jochem, L. F. Francis, S. Kumar, *Journal of Fluid Mechanics* **2022**, *938*, A22.
- [23] A. B. Appiagyei, S. Yang, J. Gu, A. Chaffee, J. Z. Liu, Q. Gu, L. Zhang, *Chem. Eng. J.* **2025**, *505*, 160684.
- [24] N. Ichikawa, K. Hosokawa, R. Maeda, *J. Colloid Interface Sci.* **2004**, *280*, 155.
- [25] C. D. Bandara, M. Schmidt, Y. Davoudpour, H. Stryhanyuk, H. H. Richnow, N. Musat, *Front. Plant Sci.* **2021**, *12*, 668929.
- [26] P. Denninger, P. Schweizer, E. Spiecker, *Micron* **2024**, *186*, 103703.
- [27] B. Gault, A. Saksena, X. Sauvage, P. Bagot, L. S. Aota, J. Arlt, L. T. Belkacemi, T. Boll, Y.-S. Chen, L. Daly, *Microsc. Microanal.* **2024**, *30*, 1205.
- [28] D. Saxey, *Ultramicroscopy* **2011**, *111*, 473.
- [29] a) E. A. Marquis, N. A. Yahya, D. J. Larson, M. K. Miller, R. I. Todd, *Mater. Today* **2010**, *13*, 34; b) M. Bachhav, F. Danoix, B. Hannover, J. M. Bassat, R. Danoix, *Int. J. Mass Spectrom.* **2013**, *335*, 57.
- [30] S. Yang, B. Qian, Y. Wang, K. Taira, Q. Zhou, K. Wilson, A. F. Lee, L. Zhang, *Appl. Catal., B* **2023**, *322*, 122106.
- [31] W. D. Rickard, S. M. Reddy, D. W. Saxey, D. Fougerouse, N. E. Timms, L. Daly, E. Peterman, A. J. Cavosie, F. Jourdan, *Microsc. Microanal.* **2020**, *26*, 750.
- [32] J. Hernández-Saz, M. Herrera, S. I. Molina, *Micron* **2012**, *43*, 643.
- [33] a) V. Deline, W. Katz, C. Evans, P. Williams, *Appl. Phys. Lett.* **1978**, *33*, 832; b) L. Li, D. S. McPhail, N. Yakovlev, H. Seng, *Surf. Interface Anal.* **2011**, *43*, 495.
- [34] C. Szakal, K. Narayan, J. Fu, J. Lefman, S. Subramaniam, *Anal. Chem.* **2011**, *83*, 1207.

- [35] C. K. Moy, G. Ranzi, T. C. Petersen, S. P. Ringer, *Ultramicroscopy* **2011**, 111, 397.
- [36] a) S. S. Rout, P. R. Heck, N. J. Zaluzec, D. Isheim, D. J. Miller, D. N. Seidman, Oxford University Press, **2018**, 26, 24; b) S.-H. Kim, K. Jang, P. W. Kang, J.-P. Ahn, J.-B. Seol, C.-M. Kwak, C. Hatzoglou, F. Vurpillot, P.-P. Choi, *J. Alloys Compd.* **2020**, 831, 154721.
- [37] a) B. Rottwinkel, A. Kreutzer, H. Spott, M. Krause, G. Schusser, T. Höche, *Microscopy Today* **2019**, 27, 40; b) J. Tang, O. Renk, M. Tkadletz, *Mater. Charact.* **2025**, 219, 114618.
- [38] J. Li, T. Malis, S. Dionne, *Mater. Charact.* **2006**, 57, 64.
- [39] F. I. Allen, P. T. Blanchard, R. Lake, D. Pappas, D. Xia, J. A. Notte, R. Zhang, A. M. Minor, N. A. Sanford, *Microsc. Microanal.* **2023**, 29, 1628.
- [40] M. Herrera, J. Hernández-Saz, N. Fernández-Delgado, L. Valencia, S. Molina, *Polym. Test.* **2023**, 128, 108232.
- [41] B. Gorman, L. Sahu, A. Shaito, D. Nandika, O. Olea-Mejia, W. Brostow, *Microsc. Microanal.* **2006**, 12, 1000.